

Guided modes of elliptical metamaterial waveguides

Klaus Halterman, Simin Feng, and P. L. Overfelt

Physics and Computational Sciences, Research and Engineering Sciences Department, Naval Air Warfare Center, China Lake, California 93555, USA

(Received 21 February 2007; published 27 July 2007)

The propagation of guided electromagnetic waves in open elliptical metamaterial waveguide structures is investigated. The waveguide contains a negative-index media core, where the permittivity ϵ and permeability μ are negative over a given bandwidth. The allowed mode spectrum for these structures is numerically calculated by solving a dispersion relation that is expressed in terms of Mathieu functions. By probing certain regions of parameter space, we find the possibility exists to have extremely localized waves that transmit along the surface of the waveguide.

DOI: [10.1103/PhysRevA.76.013834](https://doi.org/10.1103/PhysRevA.76.013834)

PACS number(s): 42.79.-e, 42.82.Et, 41.20.Jb, 42.70.Qs

Waveguides are structures that are typically designed to transmit energy along a specified trajectory with minimal attenuation and signal distortion. When transmitting surface waves, this implies confining the traveling wave within or adjacent to the waveguide walls [1]. Various avenues can be pursued when attempting to improve on a waveguides' capabilities, including modifying the constitutive effective material parameters of the guide. The recent surge of interest in negative index of refraction materials [2], or negative-index media (NIM), has prompted a reanalysis of many conventional results for waveguide devices and a subsequent search for exotic transmission characteristics when incorporating this particular composite media, or metamaterial, into a variety of waveguide configurations.

A crucial feature of NIM is the frequency dispersion of the permittivity ϵ and permeability μ , with ϵ and μ simultaneously rendered negative over a particular bandwidth. This results in wave propagation in which the phase velocity and energy flow of an electromagnetic wave can be antiparallel and also the possibility of a negative index of refraction, proposed long ago [3]. The study of various NIM based open waveguide structures and resonators during the past few years has demonstrated a number of interesting effects: it was shown [4] that a quasi-one-dimensional (quasi-1D) bilayer resonator containing a NIM layer can be substantially smaller than the usual cavity size due to phase cancellation. For the case of a thin planar NIM waveguide, the TM mode can propagate for arbitrary widths and possess a single mode for slow waves [4]. Guided TE modes were also shown to have electric field profiles containing nodes [5] and exhibit a sign-varying Poynting vector [5,6]. Similar results were reported in circular NIM fibers [7].

Distortion of the circular dielectric waveguide into an elliptical guide, while maintaining the cross-sectional area, has been shown to reduce attenuation of the dominant mode [8] and modal degeneracy, allowing for practical guiding of traveling electromagnetic waves. Attenuation effects and power flow expressions were achieved for wave propagation in a surface-wave transmission line with an elliptical cross section [9]. It was found that some modes in the guide have lower attenuation than the corresponding modes in a circular waveguide. The slow and fast hybrid-mode spectrum in a metallic elliptical waveguide with a confocal dielectric lining was also calculated [10], demonstrating the potential for a

surface-wave transmission device. Moreover, the distribution of electromagnetic fields in a double-layer elliptical waveguide was calculated to first order and revealed, in some cases, dispersion solutions where the power and phase velocity directions are antiparallel [11]. Spurred by the recent theoretical and experimental advances in NIM waveguides and resonators, we examine in this paper open NIM waveguides with elliptical cross sections, affording a greater flexibility in the parameter space determined by the geometry and material constraints. For a given eccentricity e , we calculate the permitted propagation constants over a range of frequencies. The allowed modes are separated into fast- and slow-propagating regions of the dispersion diagram, where wave localization is demonstrated in the form of electric field distributions.

When searching for exact solutions to Maxwell's equations, it is convenient to work in a coordinate system in which the boundary of the structure coincides with one of the coordinates being held constant. It is thus appropriate for the geometry under consideration to work in an orthogonal elliptical coordinate system described by the coordinates ξ and η , depicted in Fig. 1. Elliptical coordinates are related to their rectangular counterparts via $x=p \cosh \xi \cos \eta$ and $y=p \sinh \xi \sin \eta$, for $0 \leq \xi < \infty$ and $0 \leq \eta \leq 2\pi$, where p

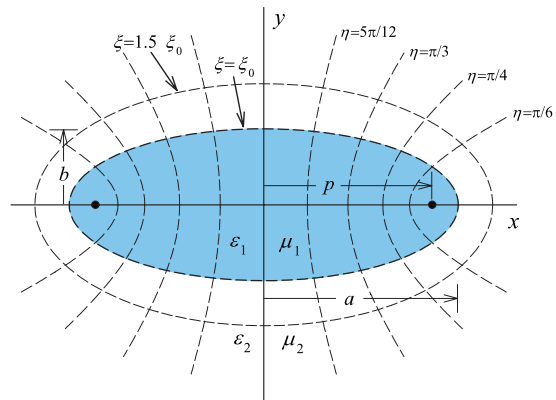


FIG. 1. (Color online) Cross section of the open elliptical waveguide structure. Within the metamaterial core, ϵ_1 and μ_1 are in general both negative and frequency dispersive. The outer region is air; $\epsilon_2=1$ and $\mu_2=1$.

$\equiv (a^2 - b^2)^{1/2}$ is the semifocal length of the ellipse expressed in terms of the semimajor and semiminor axes a and b , respectively. The waveguide boundary is located at $\xi = \xi_0$, and hence $a = p \cosh \xi_0$ and $b = p \sinh \xi_0$. It then follows that the eccentricity e is written $e = [1 - (b/a)^2]^{1/2} = 1/\cosh \xi_0$, such that $0 \leq e < 1$, with $e=0$ corresponding to a circular cross section. In order to obtain the electric (\mathbf{E}) and magnetic (\mathbf{H}) fields, we must solve the vector Helmholtz wave equation obtained from Maxwell's equations. This yields three coupled second-order differential equations for either \mathbf{E} or \mathbf{H} . The waveguide along the axial (z) direction is translationally invariant, and thus the form of the equation governing the longitudinal E_z (or H_z) is identical to the scalar Helmholtz equation in elliptic coordinates, permitting a semianalytic and more tractable solution. The fields are assumed to vary harmonically in time, and propagation occurs in the positive z direction. The wave equation then reduces to the following form:

$$\frac{1}{h^2} \left(\frac{\partial^2}{\partial \xi^2} + \frac{\partial^2}{\partial \eta^2} \right) E_{zi}(\xi, \eta) + k_i^2 E_{zi}(\xi, \eta) = 0, \quad (1)$$

where the index i denotes the region, $\sqrt{2}h \equiv p\sqrt{\cosh(2\xi) - \cos(2\eta)}$, $k_i^2 = \mu_i(\omega)\varepsilon_i(\omega)\omega^2/c^2 - k_z^2$, and for the unattenuated modes of interest here, k_z is the real propagation constant along the z direction. We have also suppressed the usual $\exp(ik_z z - i\omega t)$ factor. A similar equation exists for H_z . Due to the cylindrical symmetry, the transverse field components ($E_{\eta i}, E_{\xi i}$) and ($H_{\eta i}, H_{\xi i}$) can be determined [12] from E_{zi} and H_{zi} :

$$E_{\eta i}(\xi, \eta) = \frac{ik_z}{k_i^2 h} \left(\frac{\partial E_{zi}}{\partial \eta} - \mu_i \frac{k_0}{k_z} \frac{\partial H_{zi}}{\partial \xi} \right), \quad (2a)$$

$$E_{\xi i}(\xi, \eta) = \frac{ik_z}{k_i^2 h} \left(\frac{\partial E_{zi}}{\partial \xi} + \mu_i \frac{k_0}{k_z} \frac{\partial H_{zi}}{\partial \eta} \right), \quad (2b)$$

$$H_{\eta i}(\xi, \eta) = \frac{ik_z}{k_i^2 h} \left(\frac{\partial H_{zi}}{\partial \eta} + \varepsilon_i \frac{k_0}{k_z} \frac{\partial E_{zi}}{\partial \xi} \right), \quad (2c)$$

$$H_{\xi i}(\xi, \eta) = \frac{ik_z}{k_i^2 h} \left(\frac{\partial H_{zi}}{\partial \xi} - \varepsilon_i \frac{k_0}{k_z} \frac{\partial E_{zi}}{\partial \eta} \right). \quad (2d)$$

We proceed by inserting $E_{zi}(\xi, \eta) = U_i(\xi)V_i(\eta)$ into Eq. (1), splitting it into two ordinary differential equations with separation constant Λ :

$$\frac{d^2 V_i(\eta)}{d\eta^2} + (\Lambda - 2q_i \cos 2\eta) V_i(\eta) = 0, \quad (3a)$$

$$\frac{d^2 U_i(\xi)}{d\xi^2} - (\Lambda - 2q_i \cosh 2\xi) U_i(\xi) = 0, \quad (3b)$$

where $q_1 = (k_1 p/2)^2$ and $q_2 = -(k_2 p/2)^2$.

The angular Mathieu equation (3a) describes the angular variation of the field around the ellipse. Two linearly independent periodic solutions exist, akin to the trigonometric sin and cos functions: the even and odd angular Mathieu functions, denoted $ce_n(\eta; q_i)$ and $se_n(\eta; q_i)$, respectively. For the elliptical waveguide problem, the angular Mathieu functions must be periodic with period 2π and of integer order; otherwise the solution set is nonperiodic and can be unstable [13]. We can thus expand the angular Mathieu functions in a Fourier series, where the expansion coefficients can be found recursively by substituting the expansions back into Eq. (3a). The parameter Λ found in Eqs. (3) can be solved using a method of continued fractions [13]. The orthogonality and normalization relations of the angular Mathieu functions are given by Eq. (A1). The angular Mathieu functions are also periodic in η only for special characteristic values of Λ , denoted here as $a_n(q_i)$ for the even solutions and $b_n(q_i)$ for the odd ones.

The radial Mathieu equation (3b) admits two general types of solutions: the radial Mathieu functions of the first and second kind. The solutions of the first kind are divided into even and odd functions denoted as $Ce_n(\xi; q_i)$ and $Se_n(\xi; q_i)$, respectively. The calculation of the characteristics numbers and the Fourier coefficients is exactly the same as for the angular functions. In identifying a convenient series expansion to compute the radial Mathieu functions, a number of techniques are applicable [14]. We found, in agreement with past works, that the Bessel J_n product series are the most stable basis of functions to use [15]. Not surprisingly, the Ce_n and Se_n functions coalesce into J_n , as the elliptical cross section degenerates to a circular one. The Mathieu functions of the second kind for $q_i > 0$ are denoted $Fey_n(\xi; q_i)$ (even) and $Gey_n(\xi; q_i)$ (odd) and are calculated similarly, except the series expansion involves products of both the Bessel Y_n and J_n functions. The functions Fey_n and Gey_n are analogous to the Bessel functions of the second kind, Y_n , in circular coordinates. When $q_i < 0$, Fey_n and Gey_n transform into $Fek_n(\xi; q_i)$ and $Gek_n(\xi; q_i)$ (analogous to the Bessel K functions), and they are related [15]—e.g., for even order, $2Fek_{2n}(\xi; -q_i) = (-1)^n [-Fey_{2n}(\xi + i\pi/2; q_i) + iCe_{2n}(\xi + i\pi/2; q_i)]$.

For a general cylindrical open guide with circular cross section, pure TE or TM modes exist only for symmetrical electromagnetic fields—i.e., independent of the azimuthal angle. For an open elliptical waveguide, however, the reduction in symmetry forces the electromagnetic modes in a given region to be hybrid in that both longitudinal fields E_{zi} and H_{zi} exist simultaneously (i denotes the region). Based on the discussion above, it is clear that field solutions in an elliptical domain are split into even and odd components: $E_{zi} \rightarrow \{E_{zi}^e, E_{zi}^o\}$ and $H_{zi} \rightarrow \{H_{zi}^e, H_{zi}^o\}$. The procedure adopted here consists of writing H_{zi}^e (H_{zi}^o) waves as products involving even (odd) Mathieu functions and E_{zi}^e (E_{zi}^o) waves in terms of odd (even) Mathieu functions [8]. The complete solution is then expanded as products of angular and radial Mathieu functions of the requisite parity and that obey the radiative condition. The boundary conditions constrain the types of Mathieu functions used in the expansions [15], as we require “stationary waves” in the transverse η and ξ di-

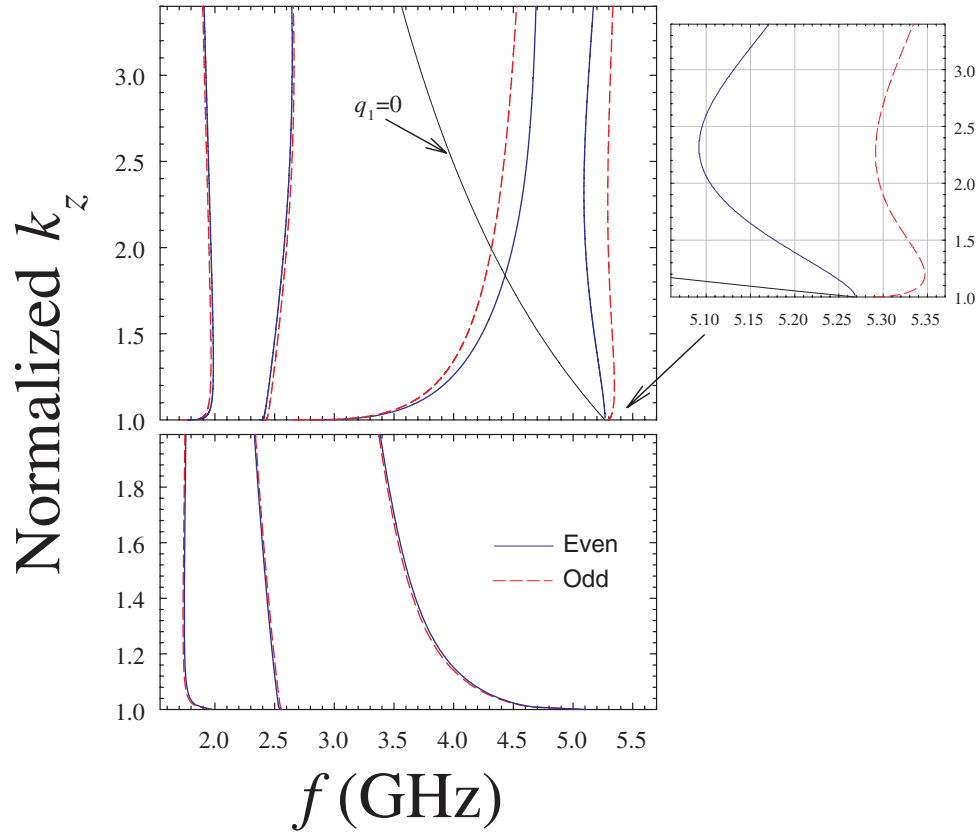


FIG. 2. (Color online) Surface-wave spectrum for the even and odd hybrid modes of an elliptical waveguide filled with NIM and embedded in air (top panel). The bottom panel is the same configuration except with positive $\varepsilon_1(\omega)$ and $\mu_1(\omega)$. The propagation constant k_z is normalized by the free-space wave number k_0 and is plotted as a function of the operating frequency for a cross section corresponding to an ellipticity of $e=0.44$. We take the characteristic frequencies in the material dispersion to be $\omega_p=8(2\pi)$ GHz and $\omega_m=7(2\pi)$ GHz, which corresponds to $\mu_1, \varepsilon_1 \leq -1$ within the frequency range $f \leq \omega_m/(2\pi\sqrt{2})$. The mode spectra illustrate the slow and fast modes, separated by the $q_1=0$ curve. If the NIM core is replaced with media corresponding to positive ε_1 and μ_1 (bottom panel), the slow-wave solution is absent and the curves vary in an opposite sense.

rection. Within each region, we thus seek solutions of the form

$$E_{z_i}^e(\xi, \eta, z) = \sum_{m=1}^{\infty} a_{mi} A_{mi}(\xi; q_i) s e_m(\eta; q_i) e^{ik_z z}, \quad (4a)$$

$$H_{z_i}^e(\xi, \eta, z) = \sum_{m=0}^{\infty} b_{mi} B_{mi}(\xi; q_i) c e_m(\eta; q_i) e^{ik_z z}, \quad (4b)$$

where a_{mi} and b_{mi} are constants and the coefficients $A_{mi}(\xi; q_i)$ and $B_{mi}(\xi; q_i)$ contain the “radial” dependence on the fields, given below. Without loss of generality, the methodology used here will focus on waves of even parity, as the procedure for odd waves is similar.

Within the waveguide region (see Fig. 1), the solutions are the radial Mathieu functions of the first kind, $A_{m1}(\xi; q_1) = S e_m(\xi; q_1)$ and $B_{m1}(\xi; q_1) = C e_m(\xi; q_1)$. For the guided modes of interest here, the fields must decay from the surface at $\xi = \xi_0$, and therefore within the surrounding medium we have $A_{m2}(\xi; q_2) \equiv G e k_m(\xi; -q_2)$ and $B_{m2}(\xi; q_2) \equiv F e k_m(\xi; -q_2)$. With this requirement on the fields and for a given set of material and geometrical parameters, a restricted number

of waveguide modes exist. To determine the allowed modes, the tangential \mathbf{E} and \mathbf{H} fields are matched at the boundary $\xi = \xi_0$ separating the two media. The η dependence is integrated out by making use of the orthogonality properties of the angular Mathieu functions (see the Appendix). We then cast the boundary-matched equations into a linear equation system containing, in principle, an infinite hierarchy of Mathieu functions. The higher-order Mathieu functions arise from the lack of a one-to-one correspondence between the angular Mathieu functions in regions with differing material parameters: the arguments of the angular Mathieu functions depend on the parameter q_i , which in turn depends on ε and μ of the relative media. This is in contrast to a circular waveguide, where the angular dependence is a function of only integer multiples of the azimuthal coordinate, $m\phi$.

In order to find the nontrivial solution, the problem of finding the allowed modes thus amounts to finding where the associated determinant of the linear equation system vanishes over a range of frequencies, propagation constants, and ellipticities. The methodology we shall discuss is valid for hybrid HE_{11} or EH_{11} (the first letter represents the dominant field) modes [8], with small e , and frequencies corresponding to small $|\varepsilon_1 - \varepsilon_2|$ (and small $|\mu_1 - \mu_2|$). Under these conditions, the expansions in Eqs. (4) can be limited to the first

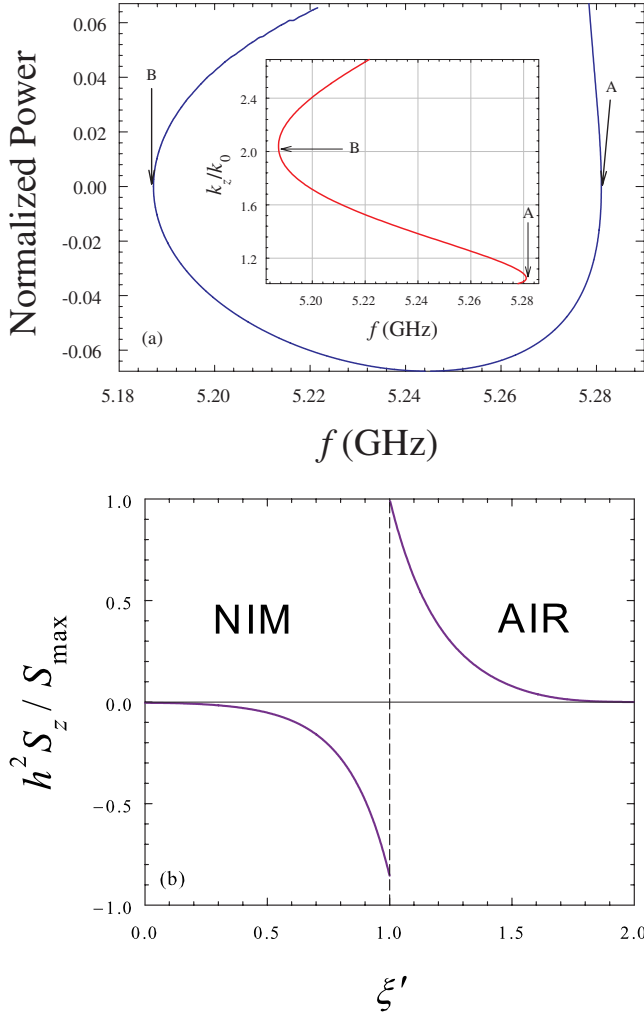


FIG. 3. (Color online) (a) The total power, $P=P_1+P_2$ (normalized by $|P_1|+|P_2|$) versus the frequency for (odd) slow wave modes. The eccentricity, e , is set at $e=0.59$. The propagation constant, k_z , increases in going from A \rightarrow B, in accordance with the mode dispersion diagram in the inset. In (b) energy-density reversal is shown by means of the Poynting vector, S_z , normalized by its maximum, and as a function of the dimensionless coordinate, $\xi' \equiv \xi/\xi_0$. The dashed vertical line identifies the NIM-air boundary. The frequency is fixed at $f=5.28$ GHz, and $k_z=1.1$. The spatial range is for the angle $\eta=\pi/6$.

few terms. Taking, for example, the two lowest-order terms in the outer region yields the following even-mode dispersion relation:

$$\begin{aligned} & \left(\frac{\varepsilon_1 Se'_1(q_1)}{q_1 Se_1(q_1)} + \frac{\varepsilon_2 Gek'_1(-q_2)}{q_2 Gek_1(-q_2)} \right) \left(\frac{\mu_1 Ce'_1(q_1)}{q_1 Ce_1(q_1)} + \frac{\mu_2 Fek'_1(-q_2)}{q_2 Fek_1(-q_2)} \right) \\ & + \frac{k_z^2}{k_0^2} \frac{1}{\alpha_{11}\beta_{11}} \left[\frac{1}{q_1 q_2} (\psi_{11} C_1 + \tau_{11} C_2) + \frac{1}{q_2} C_1 C_2 \right. \\ & \left. + \frac{1}{q_1^2} \tau_{11} \psi_{11} \right] = 0, \end{aligned} \quad (5)$$

where $k_0=\omega/c$, $C_1 \equiv -\beta_{11}\gamma_{11} - \gamma_{13}\beta_{31}$, and $C_2 \equiv \alpha_{11}\gamma_{11} + \alpha_{31}\gamma_{31}$. The quantities α_{mn} , β_{mn} , τ_{mn} , ψ_{mn} , and γ_{mn} , out-

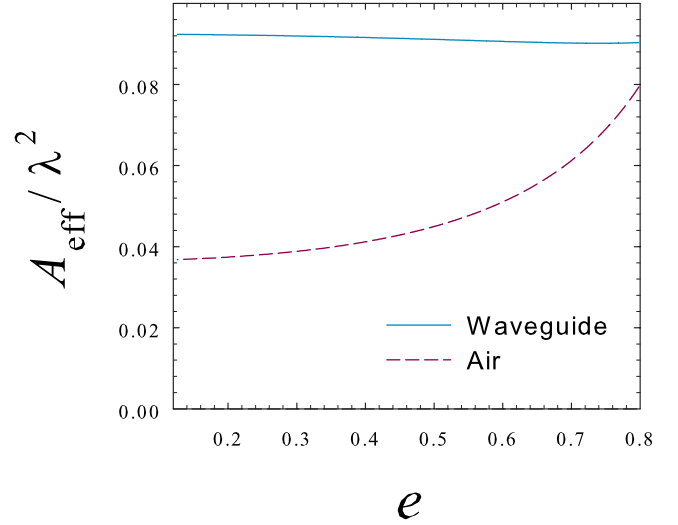


FIG. 4. (Color online) The slow-wave effective mode area A_{eff} (normalized by the wavelength λ^2) as a function of the eccentricity e .

lined in the Appendix, arise from the integrals of products of overlapping angular Mathieu functions. Writing the dispersion relation explicitly in this way reduces computational time considerably by avoiding unstable numerical determinants of large matrices and the associated multiple function calls to higher-order Mathieu functions. The odd-mode spectrum is easily obtained via the interchange $\varepsilon_i \leftrightarrow -\mu_i$. As the elliptical cross section degenerates into a circular one, $C_1 \rightarrow 1$, $C_2 \rightarrow -1$, and the Mathieu functions appropriately Bessel transform into their corresponding cylindrical Bessel functions: $\{Ce'_1(q_1)/Ce_1(q_1), Se'_1(q_1)/Se_1(q_1)\} \rightarrow uJ'_1(u)/J_1(u)$ and $\{Fek'_1(-q_2)/Fek_1(-q_2), Gek'_1(-q_2)/Gek_1(-q_2)\} \rightarrow vK'_1(v)/K_1(v)$. In this limit, the dispersion relation (5) reduces to the familiar characteristic equation for a circular waveguide:

$$\begin{aligned} & \left(\varepsilon_1 \frac{J'_1(u)}{uJ_1(u)} + \varepsilon_2 \frac{K'_1(v)}{vK_1(v)} \right) \left(\mu_1 \frac{J'_1(u)}{uJ_1(u)} + \mu_2 \frac{K'_1(v)}{vK_1(v)} \right) \\ & - \left[\frac{k_z}{k_0} \frac{(u^2 + v^2)}{u^2 v^2} \right]^2 = 0, \end{aligned} \quad (6)$$

where $u^2 = k_1^2 a^2$ and $v^2 = -k_2^2 a^2$.

The surface-wave dispersion relation (5) is a function of the parameters k_z , ω , and eccentricity e ; only particular combinations of these quantities that satisfy Eq. (5) are allowed mode solutions. The hybrid waves that are explored here can possess even and odd components, and are denoted appropriately in subsequent figures. We present the propagation constant in terms of the convenient dimensionless ratio k_z/k_0 , and the frequency units are all in GHz. The waveguide cross section is assumed to not deviate greatly from that of a circular guide, reflected in moderate values of e . The permittivity and permeability in the NIM regions, ε_1 and μ_1 , respectively, have the frequency dispersive form $\varepsilon_1 = 1 - (\omega_p/\omega)^2$ and $\mu_1 = 1 - (\omega_m/\omega)^2$, where ω_p and ω_m are the effective electrical and magnetic plasma frequencies [6], respectively.

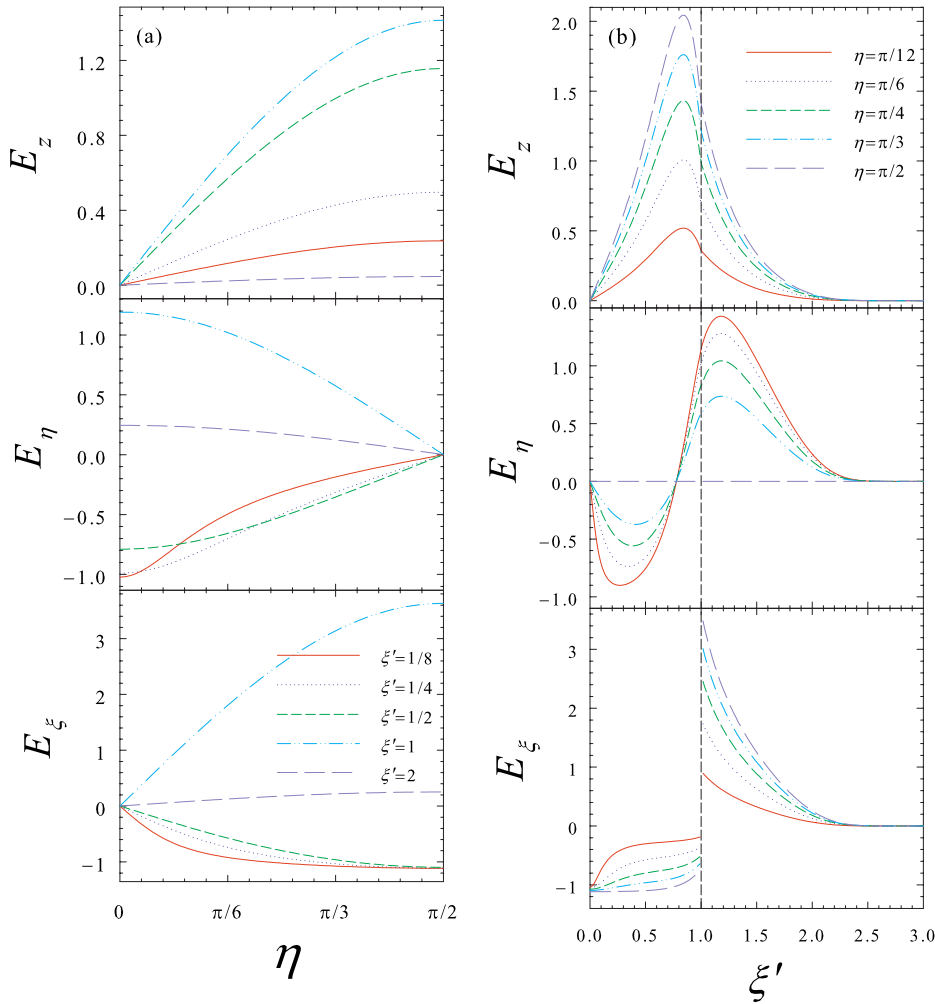


FIG. 5. (Color online) The normalized electric field distributions for even wave modes near the cutoff in an elliptical waveguide as a function of (a) angular coordinate η and (b) normalized radial coordinate $\xi' \equiv \xi/\xi_0$. The frequency is set at 3.25 GHz, and the ellipticity e has the value $e=0.14$, corresponding to $\xi_0 = 2.65$. The vertical dashed line at $\xi'=1$ identifies the waveguide boundary.

Thus for $\omega \leq \omega_p/\sqrt{2}$, we have $\varepsilon_1 \leq -1$. The study here is concerned with frequency regions of parameter space where μ_1 and ε_1 are simultaneously negative.

Determining the allowed modes typically involves holding the semimajor and semiminor axes of the waveguide (and hence e) fixed and then scanning Eq. (5) over k_z and ω . Any sign change that occurs signifies a zero crossing that can be pinpointed through an iterative root-finding process. Other variable combinations may be used, depending on the parameter study. In the top panel of Fig. 2 we show the mode spectra found by solving Eq. (5), and its odd counterpart, for a waveguide with eccentricity $e=0.44$. For clarity, only four neighboring sets of dispersion curves within the given frequency window are shown. Two sets reside completely beneath the $q_1=0$ curve, one set entirely outside of it, and another set that traverses both regions. For this geometry and range of frequencies, the paired even-odd-mode solutions follow similar trends, separating at higher frequencies. The solutions to the Helmholtz equation (1) depend on the eccentricity e of the elliptical guide through the parameters q_1 and q_2 . We found as the ellipse flattens, more splitting occurs between the even and odd modes. In general, each branch of the even and odd modal curves coalesce at cutoff, where the propagation constant approaches the free-space value ($k_z \rightarrow k_0$). The dispersion diagram portrays the allowed electromagnetic-wave solutions that travel along the guide,

and it elucidates important information regarding the possible localization characteristics of guided modes. In particular, the first three sets of dispersion curves that satisfy $\sqrt{\varepsilon_2 \mu_2} \leq k_z/k_0 \leq \sqrt{\varepsilon_1 \mu_1}$ correspond to conventional surface waves. Within this parameter space region, the phase velocity of guided waves, v_p , exceeds the phase velocity of waves in a homogeneous bulk medium—i.e., $v_p > c/\sqrt{\varepsilon_1 \mu_1}$. These *fast-wave* solutions to Maxwell's equations will decay in the air region, but not necessarily in the waveguide core. Indeed, as the structure increases in size, or as f decreases (increasing $|\varepsilon_1|$), the electric and magnetic fields inside the waveguide oscillate with shorter wavelengths. At the cutoff, $k_2 \rightarrow 0$ (thus $q_2 \rightarrow 0$), and the ensuing decay length increases outside the guiding surface. This causes a significant portion of the energy flow to occur in the air region, where the fields can then become less sensitive to the relevant geometrical parameters, such as the ratio a/b .

We see in Fig. 2 that for the case of a NIM core, there are also solutions that reside outside of the $q_1=0$ boundary. These *slow-wave* solutions are noticeably absent when ε_1 and μ_1 are strictly positive (see bottom panel). The presence of NIM sets up a nonoscillatory field profile that rapidly decays outside the guide, allowing for the possibility of guided modes that are more localized to the surface, akin to surface plasmon waves on metal surfaces studied long ago. Note that as k_z increases, q_2 typically increases, in which

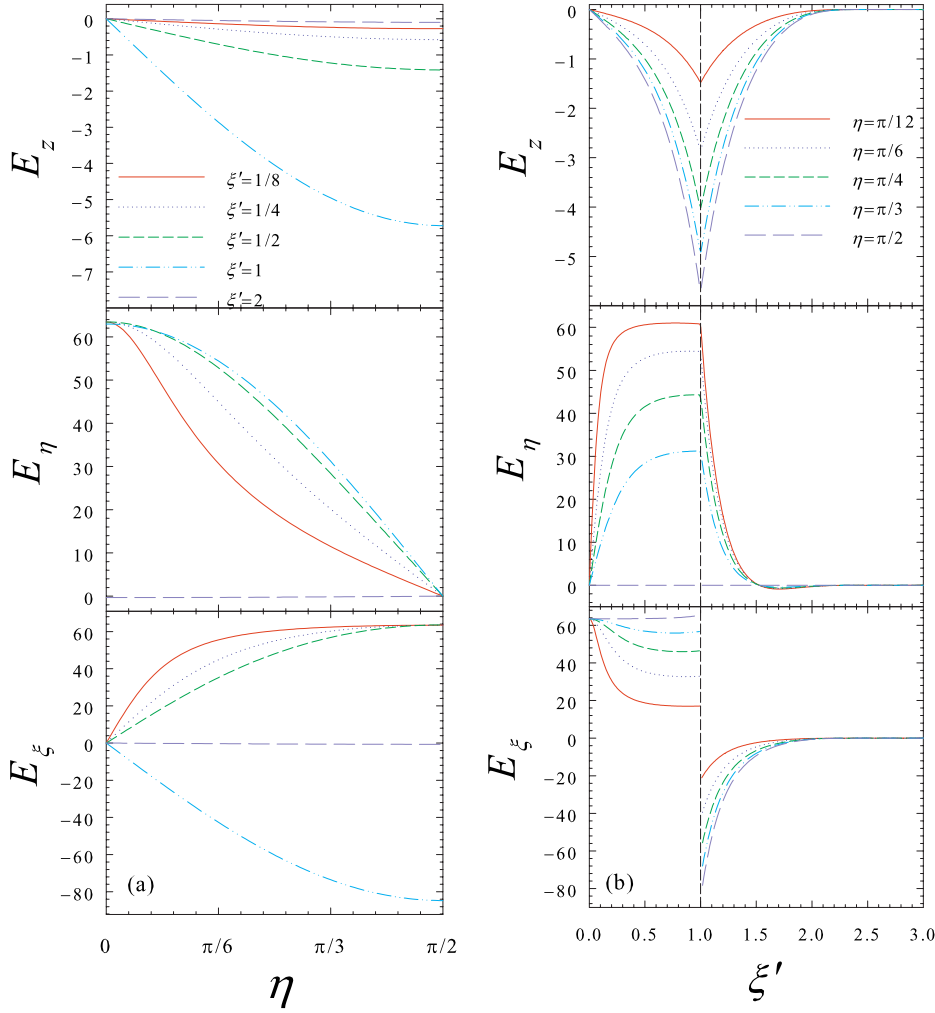


FIG. 6. (Color online) The spatial and angular variation of the electric field, with the same parameters as in Fig. 5, except at the higher frequency, $f = 5.28$ GHz. These localized slow waves decay away from the outer side of the interface rapidly, consistent with dispersion curves of Fig. 2.

case the radial Mathieu functions decay sharply, confining the field more to the waveguide. The slow-wave solutions seen in the inset of Fig. 2 have dispersion characteristics that depend strongly on frequency. Near the cutoff, these modes demonstrate that the direction of the group velocity, $d\omega/dk_z$, evaluated at a particular k_z , can differ among the even- and odd-wave solutions. This is related to the (time-averaged) local energy-density flow along z , $S_{zi} = (1/2)\text{Re}(E_{\xi i} H_{\eta i}^* - E_{\eta i} H_{\xi i}^*)$. An excited wave with the appropriate frequency can reverse direction between layers, a hallmark of the peculiar wave propagation that can arise in NIM guiding structures. To address the relationship between net energy flow in the system and group velocity, we show in Fig. 3(a), the total power P as a function of the calculated mode frequency, found by summing the power flow in the waveguide (P_1) and air (P_2) regions. The power through a given cross-sectional area A was calculated by integrating the z component of the Poynting vector over A ,

$$P_i = \iint_A S_{zi} h^2 d\eta d\xi, \quad i = 1, 2, \quad (7)$$

where h is the usual coordinate scale factor. The frequencies used in determining P are governed by the dispersion curve, shown in the inset of Fig. 3(a). The arrows label points

where $d\omega/dk_z$ is zero in the dispersion diagram and correlate with zero net power flow in the system—i.e., $P_1 = -P_2$. In general, we see from the figure that the direction of net power flow coincides with the sign of $d\omega/dk_z$. A sign change in this slope causes the dispersion curves to bend back in the k_z - ω plane, related to the P_1 and P_2 sign difference, which can yield a sum ranging from positive to negative, depending on their relative values. The bottom panel (b) shows the spatial dependence of the energy-density flow and its associated reversal in going from NIM to air.

We now characterize mode localization with an effective mode area A_{eff} , defined as the ratio of the electromagnetic energy to the maximum value of the energy density,

$$A_{\text{eff}} \equiv \frac{\int \int_A U(\xi, \eta) h^2 d\eta d\xi}{U_{\text{max}}(\xi, \eta)}, \quad (8)$$

where the energy density U for frequency-dispersive materials is defined as [16]

$$U(\xi, \eta) = \frac{1}{8\pi} \left[\frac{d(\omega\epsilon)}{d\omega} |\mathbf{E}|^2 + \frac{d(\omega\mu)}{d\omega} |\mathbf{H}|^2 \right]. \quad (9)$$

The normalized effective mode area for slow waves near the cutoff ($k_z/k_0 = 1.01$) is shown in Fig. 4 as a function of the eccentricity e . The mode frequencies calculated from Eq. (5)

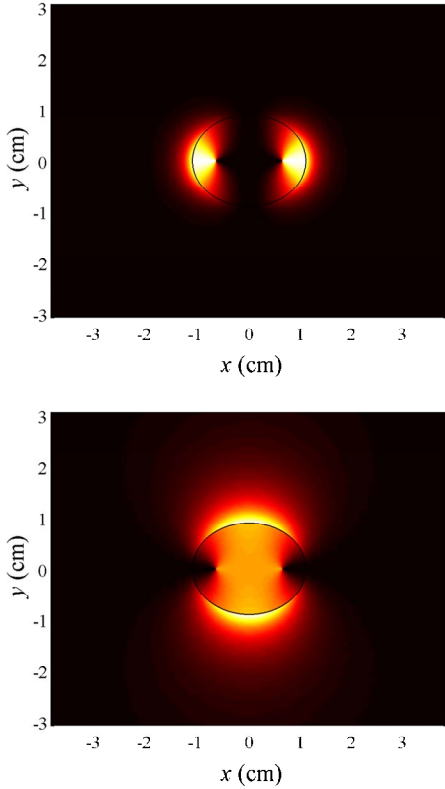


FIG. 7. (Color online) Contour plots of the even transverse electric field amplitudes for $e=0.59$ and $f=5.3$ GHz. The top and bottom panels correspond to E_η and E_ξ , respectively. Bright areas indicate larger field intensities. Each component is normalized to its respective maximum for clarity.

are a weak function of e over the range shown. We see that A_{eff} in the air region tends to decrease as the guide becomes more circular, while within the guide, the effective area is nearly constant. Thus, as a circular guide is slightly distorted into an ellipse, the exhibited mode localization properties within the NIM structure remain rather robust.

To gain insight into the transmission properties of an elliptical NIM waveguide excited by a particular source, the spatial and angular features of the EM field components are essential. We therefore show in Fig. 5 the three components of the \mathbf{E} field near the cutoff and at a frequency corresponding to $\varepsilon_1=-5.04$ and $\mu_1=-3.63$. The cross-sectional area πab of the waveguide is held fixed with $e=0.14$. The left panel, Fig. 5(a), illustrates the normalized \mathbf{E} field as a function of η for five different values of the normalized coordinate, $\xi' \equiv \xi/\xi_0$. The right set of figures, Fig. 5(b), exhibits the normalized electric field as a function of ξ' for five different η . Parenthetically, in comparing field distributions with a circular waveguide, one can scale the coordinates (e.g., for $\eta=\pi/2$): $\xi \rightarrow p \sinh \xi$. From panel (a), we see that the longitudinal E_z and “radial” E_ξ components have the expected behavior along the semimajor axis, since the η dependence to those fields involves $se_m(\eta; q_i)$ and $ce'_m(\eta; q_i)$ terms, which vanish at $\eta=0$. Likewise, E_η is comprised of products involving $ce_m(\eta; q_i)$ and $se'_m(\eta; q_i)$ functions, and hence tends toward zero for positions along the semiminor axis ($\eta=\pi/2$). Turning to the ξ dependence in panel (b), it is

evident that within the waveguide region, for $\xi=0$ (along the line $x'=p \cos \eta$), the z and η components to the field vanish, while E_ξ has its maximum there. It is apparent that, on average, each of the components is similar in magnitude, with E_ξ dominating slightly over the others in some instances. Another distinguishing feature among the components is the shifting of the peak intensity of the field patterns: E_z reaches its peak value inside of the waveguide, and E_η has its largest value just outside the core boundary, while E_ξ peaks out along the waveguide walls ($\xi'=1$), after which it undergoes a discontinuous transition. This behavior is consistent with the boundary condition $\Delta E_\xi(\xi_0)=(1-\varepsilon_1/\varepsilon_2)E_{\xi 1}(\xi_0)$.

To explore the possibility of field localization in the slow-wave regime, Fig. 6 illustrates the localized slow-wave solutions as a function of η and ξ . The frequency chosen, 5.28 GHz, lies just outside the $q_1=0$ curve at $k_z/k_0 \approx 1.01$ and approximate frequency (in GHz),

$$f \approx \frac{\omega_p \omega_m}{2\pi \sqrt{\omega_m^2 + \omega_p^2}} \left(1 - \frac{[(k_z/k_0)^2 - 1] \omega_m^2 \omega_p^2}{2(\omega_m^2 + \omega_p^2)^2} \right) = 5.26. \quad (10)$$

Examining the interior of the waveguide, Fig. 6(b) is consistent with Fig. 5(b) at $\xi=0$, where only E_ξ survives before declining towards the interface. As $\eta \rightarrow \pi/2$, E_ξ becomes more weakly dependent upon the coordinate ξ , while if $\eta \rightarrow 0$, E_ξ and E_z vanish and E_η approaches a constant value within the guide. The \mathbf{E} field components transverse to the direction of energy flow, E_η and E_ξ , clearly dominate here, and thus the behavior of these particular modes is quite relevant in the determination of waveguide transmission capabilities. It is further evident from Fig. 6(b) that the length scale of field decay in the air region is at times shorter, demonstrating that the possibility exists to tailor the guide or feed line in a way that transmits ultralocalized waves.

The dominant transverse electric field profiles mapped onto a Cartesian coordinate system are shown in Fig. 7. The 2D contour plots are consistent with the field patterns exhibited in Fig. 6.

In conclusion we have shown that elliptical waveguides with NIM can support both fast- and slow-wave modes. The power flow in the system was shown to have direct correlations with the group velocity: points on the dispersion curves where the group velocity is zero corresponded to zero net power flow through the entire structure. The Poynting vector was shown to reverse when crossing the boundary between air and NIM. The dispersion relation was shown to admit localized solutions that retain their characteristics under moderate variations of the eccentricity.

This project is funded in part by the Office of Naval Research (ONR) In-House Laboratory Independent Research (ILIR) Program and by a grant of HPC resources from the Arctic Region Supercomputing Center at the University of Alaska Fairbanks as part of the Department of Defense High Performance Computing Modernization Program.

APPENDIX: OVERLAP INTEGRALS OF ANGULAR MATHIEU FUNCTIONS

When matching the tangential fields at the boundary, the orthogonality properties of the angular Mathieu functions

give rise to several overlap integrals, given as

$$\alpha_{mn} = \frac{1}{\pi} \int_0^{2\pi} d\eta c e_m(\eta; -q_2) c e_n(\eta; q_1), \quad (\text{A1a})$$

$$\beta_{mn} = \frac{1}{\pi} \int_0^{2\pi} d\eta s e_m(\eta; -q_2) s e_n(\eta; q_1), \quad (\text{A1b})$$

$$\tau_{mn} = \frac{1}{\pi} \int_0^{2\pi} d\eta s e'_m(\eta; q_1) c e_n(\eta; -q_2), \quad (\text{A1c})$$

$$\psi_{mn} = \frac{1}{\pi} \int_0^{2\pi} d\eta c e'_m(\eta; q_1) s e_n(\eta; -q_2), \quad (\text{A1d})$$

$$\gamma_{mn} = \frac{1}{\pi} \int_0^{2\pi} d\eta c e'_m(\eta; -q_2) s e_n(\eta; -q_2). \quad (\text{A1e})$$

When $q_1 = q_2$, $\beta_{mn} = \delta_{mn}$, and $\alpha_{mn} = \delta_{mn}$. In the limiting case of the ellipse reducing to a circle, then we also have $\tau_{mn} \rightarrow m\delta_{mn}$ and $\psi_{mn} \rightarrow -m\delta_{mn}$, and $\gamma_{mn} \rightarrow -m\delta_{mn}$. In all cases, the integrals are zero if the m is even and n is odd or vice versa, due to the symmetry properties of the products of periodic Mathieu functions.

-
- [1] N. S. Kapany and J. J. Burke, *Optical Waveguides* (Academic Press, New York, 1972).
- [2] J. B. Pendry, *Phys. Rev. Lett.* **85**, 3966 (2000).
- [3] V. G. Veselago, *Sov. Phys. Usp.* **10**, 509 (1968).
- [4] N. Engheta, *IEEE Antennas Wireless Propag. Lett.* **1**, 10 (2002); A. Alu and N. Engheta, *IEEE Trans. Microwave Theory Tech.* **52**, 199 (2004).
- [5] I. V. Shadrivov, A. A. Sukhorukov, and Y. S. Kivshar, *Phys. Rev. E* **67**, 057602 (2003).
- [6] K. Halterman, J. M. Elson, and P. L. Overfelt, *Opt. Express* **11**, 521 (2003).
- [7] A. V. Novitsky and L. M. Barkovsky, *J. Opt. A, Pure Appl. Opt.* **7**, S51 (2005).
- [8] C. Yeh, *J. Appl. Phys.* **33**, 3235 (1962).
- [9] S. R. Rengarajan and J. E. Lewis, *IEEE Trans. Microwave Theory Tech.* **28**, 1085 (1980).
- [10] S. R. Rengarajan and J. E. Lewis, *IEEE Trans. Microwave Theory Tech.* **28**, 1089 (1980).
- [11] S. B. Rayevskiy, L. G. Simkina, and V. Ya. Smorgonskiy, *Radiotekh. Elektron. (Moscow)* **18**, 985 (1973).
- [12] J. D. Jackson, *Classical Electrodynamics*, 2nd ed. (Wiley, New York, 1975), p. 341.
- [13] J. C. Gutiérrez-Vega, R. M. Rodríguez-Dagnino, M. A. Meneses-Nava, and S. Chávez-Cerda, *Am. J. Phys.* **71**, 233 (2003).
- [14] *Handbook of Mathematical Functions*, edited by M. Abramowitz and A. Stegun (U.S. GPO, Washington, D.C., 1964).
- [15] N. W. McLachlan, *Theory and Applications of Mathieu Functions* (Dover, New York, 1964).
- [16] L. D. Landau and E. M. Lifshitz, *Theoretical Physics: Electrodynamics of Continuous Media* (Pergamon Press, Oxford, 1960).